Corrosion Science 185 (2021) 109327

Contents lists available at ScienceDirect

Corrosion Science

journal homepage: www.elsevier.com/locate/corsci

High temperature oxidation of higher manganese silicides

Antoine de Padoue Shyikira [a,*], Naureen Akhtar [a], Gunstein Skomedal [a,b], Tor Oskar Sætre [a], Peter Hugh Middleton [a]

[a] University of Agder, Norway
[b] Elkem ASA –Kristiansand, Norway

ARTICLE INFO

Keywords:
Higher manganese silicides
High temperature corrosion
Selective oxidation
Silicide thermoelectric materials
Microstructures

ABSTRACT

The oxidation kinetics and mechanisms of higher manganese silicides (HMS) $MnSi_{1.75}$, $MnSi_{(1.75-x)}Ge_x$, $MnSi_{(1.75-x)}Al_x$ (with x = 0.005 and 0.01)were studied and the effects of densification methods and dopant concentration discussed. Oxidation experiments were conducted using thermogravimetry (TGA), while post characterization with X-ray Photoelectron Spectroscopy (XPS) and Scanning Electron Microscope (SEM) showed that spark plasma sintering (SPS) is a better densification method than hot pressing (HP). Except for undoped HMS, HMS doped with 0.5at% Ge had the lowest oxidation rate. Stable formation of a SiO_2 protective layer was the main reason for improved oxidation resistance in air in the temperature range 200 °C–500 °C.

1. Introduction

Stochiometric $MnSi_x$ (with $1.71 \leq x \leq 1.75$) alloys [1,2] are among the most promising p-type silicide thermal electric materials. The interest stems mainly from the relatively high abundance of the main constituent elements (with Si 2nd and Mn 12th), low cost, mechanical and chemical stability, low toxicity, and ease of production [3]. However, pure HMS has a relatively low thermoelectric figure of merit (zT), ranging from 0.3−0.5 at temperatures below 500 °C [3,4]. For decades, researchers have been working to improve the zT values by optimizing the electrical transport properties and decreasing the lattice thermal conductivity [5]. In particular Biernert and Gillen [6], a decent improvement has been reached through optimization of synthesis and consolidation parameters [7,8], Nanostructuring [2,9], phase engineering, and electronic engineering.

Among HMS dopants candidates, aluminium (Al) [10], and germanium (Ge) [11,12] have been reported as the most effective substitutes of Si on the silicon site. Dharmaiah et al. [13] reported a thermal conductivity decrease by 25 %, with Ge as a substitution on the Si site ($MnSi_{1.75-x}$ Ge_x), which attributed to increased phonon scattering by pores and voids, and the figure of merit (zT) increased up to 0.6 [12] and 0.62 at 560 °C [14]. Moreover, Luo et al. [10] studied the $MnSi_{1.80-x}Al_x$ alloys with $0 \leq x \leq 0.009$, where an optimal and increased charge carrier concentration was observed at x = 0,0015 with 0.65 (zT) at 527 °C. However, adding impurities can make the alloy more prone to oxidation [15] or oxidation resistant [16,17].

Along with improving the thermoelectric properties of HMS alloys, a parallel oxidation study is important while designing the thermoelectric material. $MnSi_x$ are relatively stable up to 600 °C in oxidative atmospheres [18], however doping or alloying with reactive elements, causes the oxidation state to vary with the dopant type and concentration [19]. Few HMS oxidation studies have been carried out at temperatures above 1000 °C, and even fewer below 600 °C. Ning et al. [20], studied the oxidation of uncoated and glass ceramic coated $MnSi_{1.74}$ at 600 °C for 500 h in air. The uncoated samples grew a SiO_2 layer of 5 μm with a Si depleted region (MnSi) of the same thickness and the same trend was observed by Funahashi et al. [21], although they had carried out their tests for a short period of 10 h. Likewise, they also observed that their uncoated sample showed a decrease in the Seebeck coefficient as well as a decrease in the electronic conductivity both of which implied a lower power factor compared to "as-sintered" samples. However, coated samples showed resistance to oxidation and retained the same power factor after heat treatment.

Similarly, M. Salvo et al. [22], studied the thermal oxidation of HMS and included thermal cycling in their testing procedures comprising of 10 cycles with 1 h dwell time from ambient to 600 °C in air. With XRD they observed Mn_2O_3 and some SiO_2(cristobalite)in the sub-surface. Si has a high affinity to oxygen relative to Mn, however the silicon concentration in the depleted region at the alloy-oxide may reach a minimum, thus Mn contributes to the oxide formation. This was discussed by

* Corresponding author.
E-mail addresses: tonnydepadoue15@gmail.com, antoine.d.shyikira@uia.no (A.P. Shyikira).

https://doi.org/10.1016/j.corsci.2021.109327
Received 21 September 2020; Received in revised form 12 February 2021; Accepted 13 February 2021
Available online 18 February 2021

X. j.Liu et al. [23] regarding the oxidation of Fe-Si alloys, where they revealed the effect of the silicon content and temperature on oxidation of Fe-Si and confirmed Wagner's theory of oxide structure between two oxidation-prone elements.

For further and better understanding of the oxidation robustness of HMS and its alloys, thermal oxidation of $MnSi_{1.75-\alpha}X_\alpha$ (X: Ge or Al) alloys was studied in the intermediate (300 °C −500 °C) and high (600 °C) temperature ranges. This study mainly discusses the effect of temperature, optimal dopant concentration, and consolidation methods on oxidation of the investigated compounds. Moreover, the dopants being reactive to oxygen, the so-called "third element effect" [24] is discussed based on SiO_2 – GeO_2/Al_2O_3 oxides coexistence.

2. Experimental

2.1. Material and bulk specimen preparation

HMS alloys synthesized from different compositions of Silicon and Manganese, doped with Al and Ge at the silicon site (see Table 2 for nominal composition) were synthesized by Elkem ASA [25]. The raw materials were mixed, melted in an induction furnace under argon atmosphere, and then cast in a graphite mould. The ingots were crushed, and ball milled down to micron-sized powder, using a Herzog HSM 100 vibratory mill. Sample pellets were then made from the powder and sintered by Spark Plasma Sintering (SPS) (Dr. Sinter, SPS-825 – NTNU-Trondheim) and conventional Hot Pressing (HP) (homemade vertical HP – University of Oslo) to produce 30−36 mm diameter x5 mm discs. These were cut to size (1 × 3 × 4 [mm]) with a diamond cut-off wheel (Struers), mechanically ground and polished using SiC paper (up to 2400grit paper), and diamond suspensions (from 9 μm to 1 μm), respectively. Finally, the samples were ultrasonically cleaned in acetone for 3 min and rinsed in acetone before carrying out the analytical work.

2.2. Thermal treatment

The thermal oxidation experiments were conducted using a thermogravimetric analyzer (TGA/DSC 1, Mettler Toledo) in both ambient air and dry air. The powder samples (before densification) were put in 150 μL alumina crucibles for iso-conversion tests from 25−1000 °C, with 5 °C/min constant heating rate, and 50 mL/min reaction gas purging rate. For isothermal experiments, the pressed discs of HMS were heat-treated at 300 °C, 350 °C, 400 °C, 450 °C/500 °C, and 600 °C for 15 h/24 h, 72 h, and 200 h.

2.3. Characterization and micro-structure

2.3.1. Oxidation kinetics

To determine the kinetic behaviour, the empirical model derived by Pilling and Bedworth was used, in which the experimental weight gain per unit area of the sample is plotted against time during a constant heating rate supplied to the apparatus (Eq. (1)) [26]. From this analysis, the parabolic oxidation rate can be determined.

$$\frac{\left(m_{oxide}/A\right)^n}{t} = k_p \tag{1}$$

Where: m_{oxide} - stand for the mass of oxide, A – the surface area of the specimen, t – time, and k_p is the oxidation rate. Similarly, following the Arrhenius oxidation model [27,28], the relationship between the oxidation rate and the temperature is expressed by Eq. 2 which enables the sample oxidation activation energy (E_p) to be calculated (see Fig. A3).

$$k_p = k_0 e^{\left(-E_p/RT\right)} \tag{2}$$

Where: k_0 – is the pre-exponential factor; R and T: the gas constant and temperature, respectively; and E_p – is the oxidation activation energy. Finally, the oxide thickness (x_{oxide}) is approximated by Eq. 3, where ρ_{oxide} represent the oxide density (with SiO_2 assumed to be the sole oxide).

$$x_{oxide} = \frac{m_{oxide}/A}{\rho_{oxide}} \tag{3}$$

2.3.2. Composition

The residues of the oxidized powder samples were experimentally characterized by X-ray photoelectron spectroscopy (XPS). The data were collected with a Kratos Axis Ultra^{DLD} spectrometer using a monochromatic Al KαX-ray source (1486.6 eV) operated at 10 A and 15 kV. Pass-energies of 160 eV and 40 eV were used for the survey spectra and the detailed core-level spectra, respectively. The energy step sizes of 1 eV and 0.1 eV were chosen for the survey and the detailed core-level spectra, respectively. Binding energies were referenced to the C 1s photoemission peak centred at 284.8 eV for adventitious carbon absorbed on the sample surface. A detailed analysis of the XPS data was

Table 1
Overview of all raw materials feedstock used in synthesis (wt%).

	ESS	Silgrain HQ	Mn	LC-SiMn
Source	REC Solar	Elkem	Alfa Aeser	Eramet
Shape	~1 mm powder	0.2−0.8 mm powder	1−10 mm flakes	
Si	>99.999	>99.8	1.3	29.47
Mn	–	–	>98.5	59.25
Fe	<0.0001	0.04	–	10.55
Al	<0.0001	0.09	–	–
Ti	<0.0001	0.001	–	0.293
Ca	<0.001		–	0.005
P	<0.0001	0.002	–	0.096
B	<0.0001	0.003	–	–
C	–	–	0.007	0.036
Cr + Co + Ni + Cu				~0.2

Table 2
List of samples ID, nominal composition, and synthesis routes.

Sample ID	Nominal composition	Synthesis
HMS_a	$MnSi_{1.75}$	α, σ, τ
HMS_b	$MnSi_{1.75}$	α
HMS_c	$MnSi_{1.75}$	γ
Ge0.5_c	$MnSi_{1.745}Ge_{0.005}$	γ, σ
Ge1_c	$MnSi_{1.74}Ge_{0.01}$	γ
Al0.5_c	$Mn_{0.99}Si_{1.745}Al_{0.005}$	γ
Al1_c	$Mn_{0.99}Si_{1.74}Al_{0.01}$	γ
Ge0.5_b	$MnSi_{1.745}Ge_{0.005}$	α, τ
Ge1_b	$MnSi_{1.74}Ge_{0.01}$	α, σ
Al0.5_b	$Mn_{0.99}Si_{1.745}Al_{0.005}$	α, τ
Al1_b	$Mn_{0.99}Si_{1.74}Al_{0.01}$	α

α: Melting (1450 °C) + casting; **γ:** Melting (1600 °C) + casting; **σ:** hot pressing (850 and/or 950 °C); **τ:** SPS (850 °C).

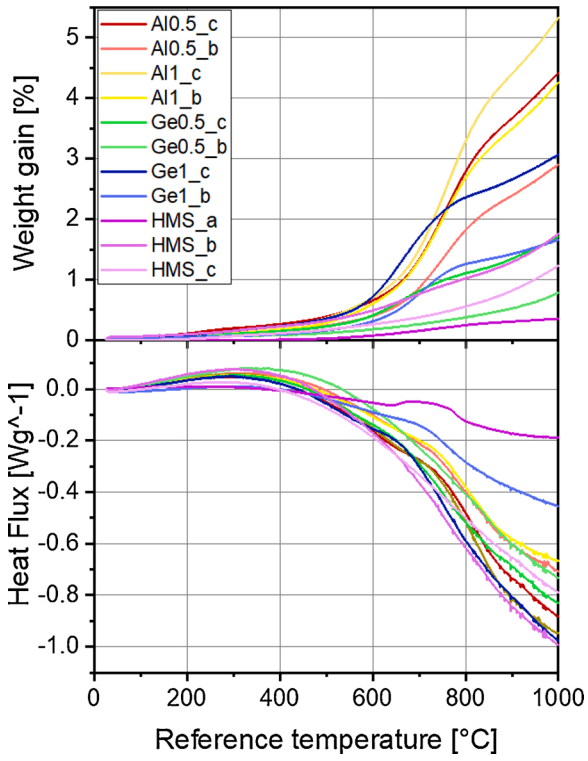

Fig. 1. Top: Thermogravimetric weight change of HMS alloys (powder samples) oxidized in air from 25 °C -1000 °C by TGA/DSC 1, Bottom: Differential scanning calorimetric (DSC) representation of the alloys presented on top, respectively.

performed using the least square fitting program Winspec developed at the LISE, University of Namur, Belgium. Peak fitting of the XPS spectra involved the subtraction of a Shirley type background and peak deconvolution using a linear combination of Gaussian and Lorentzian functions. The spectra were deconvoluted into the least number of components, which gives a good fit of the experimental data.

2.3.3. Microstructure analysis

The microstructures of the oxidized and non-oxidized specimen were imaged using a scanning electron microscope (SEM, Zeiss Merlin) equipped with an energy dispersive X-ray spectrometer (EDS). The microscope was operated at 15 kV (accelerating voltage), and the working distance ranging from 5 to 5.6 mm. From backscattered images, oxide phase composition was detected by EDS and analysed by elemental mapping and line scan using ESPRIT software from BRUKER.

3. Results

3.1. Constant heating rate

3.1.1. Thermogravimetric analysis

In the beginning, all powder samples (Table 2) were oxidised in the air from 25 °C -1000 °C at 5 °C/min using TGA. Fig. 1 shows that in general, the weight gain of all samples begins in the temperature range between 200−400 °C with a very slow oxidation rate. Undoped HMS (a, b, and c) show more robustness to oxidation relative to doped HMS, with total weight gain averaging between 0.35 % and 1.75 % corresponding to HMS_a and HMS_b, respectively.

Furthermore, the HMS alloys investigated were Ge and Al-doped with 0.5–1 at% dopant concentration, represented by subscript “b” and “c”. The TGA weight change Fig. 1, shows that all alloys of batch “c” oxidized at a much higher rate than the ones in “b”. From the synthesis route presented in Table 2, the two batches are distinct only from the melting temperature. The microstructure of the compounds (see Fig. 2) revealed that batch c had a high amount of SiC precipitates and a substantial amount of MnSi secondary phase, conversely batch b has a high amount of MnSi phase, and less SiC precipitates. The SiC formation during melting and casting originates from the reaction of the melt and the graphite crucible. Moreover, it is seen how the samples with higher Ge and Al amount results in a more heterogeneous microstructure. With increasing Al or Ge, the amount of MnSi phases (light grey) increases substantially. In addition, Ge doped samples have Ge precipitate phases with the amount increasing with higher dopant concentration. Also, slight amounts of SiC in samples batch a, and c – e are seen, while sample b shows Si phase around the grain boundaries.

Between 600 °C and 800 °C, the Ge and Al-doped powders oxidised much faster than undoped HMS, the increase in oxidation rate is associated with the reactivity of the dopant towards oxidation. The results revealed that the doped HMS compounds oxidation kinetics depends on the dopant type and concentration, where Al-doped alloys have the highest oxidation rate, hence higher weight gain of 5.33 % (1 at% Al) and 4.2 % (0.5 at% Al). A similar trend can be seen on Ge doped alloys, though the oxidation rate is around half that of Al-doped alloys.

3.1.2. Oxide composition

The composition of the oxidised powder at 1000 °C was carried out using XPS to investigate the different species that were formed as a result of the oxidation process in the undoped and the doped samples. Fig. 3 displays the high-resolution spectra of Mn 2p, Si 2p, O 1s, Al 2p, and Ge 2p core lines. The Mn 2p spectra showed two distinct peaks at ~ 642 eV and ~ 654 eV assigned to the 3/2 and 1/2 spin-orbit splitting components, respectively. The binding energy of the main peaks is indicative of the manganese in the higher-oxidation state (Mn^{4+}) [29]. Manganese forms oxide species in at least three oxidation states, Mn^{2+}, Mn^{3+}, and Mn^{4+} which exhibit significant multiplet splitting [30,31]. These multiplet splitting structures have overlapping binding energies that make it challenging for quantitative analysis. However, Mn 2p spectra also showed a shoulder at the higher binding energy side at ~ 646 eV, characteristic of Mn^{2+} [30,32]. This suggests that the Mn-oxide also contains MnO, besides MnO_2. However, the quantification of each type is not straightforward due to similar binding energies [31].

The Si 2p XPS spectra showed an intense peak centred at 103.7 eV and a small feature at the low binding energy side (~ 102 eV) as indicated by an arrow. The main peak is assigned to Si^{4+} while low binding energy is indicative of Si in the low-oxidation state (3+) [33]. The O 1s spectra also displayed two main features where a high binding energy component is consistent with Si-oxide [33], while low binding energy component is representative of Mn-oxide [34]. The observed binding energies of Al 2p and Ge 2p core-level spectra identify the presence of Al_2O_3 [35] and GeO_2 [36].

A more detailed analysis of Si 2p and O 1s core-level spectra is displayed in Figs. 4 and 5 respectively. These results show that oxidation results in the formation of SiO_2 as the main phase. In Fig. 4, the integrated area under the peak for the low binding energy component (Si^{3+}) is 3.7 % (for undoped compound) that of the total spectrum and increases with Al doping (up to 8.0 %). However, this component is not present in a Ge doped sample where Si exists in 4+ oxidation state only.

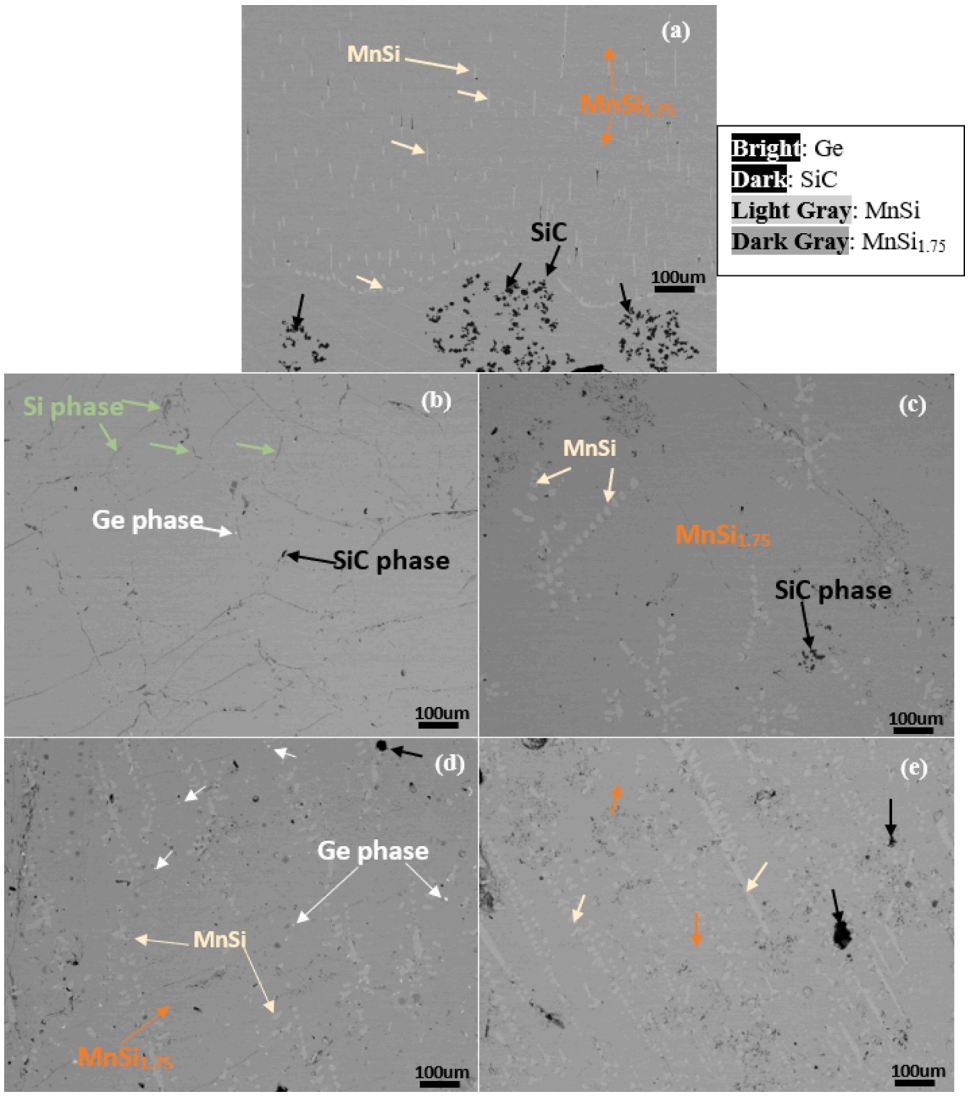

Fig. 2. SEM - backscattered electron images on cross-section of alloys (a) $MnSi_{1.75}$, (b) $MnSi_{1.745}Ge_{0.005}$, (c)$MnSi_{1.745}Al_{0.005}$, (d) $MnSi_{1.74}Ge_{0.01}$, and (e)$MnSi_{1.74}Al_{0.01}$, showing large variation in microstructure with different additions of Ge and Al. With increasing Al or Ge, the amount of MnSi phases (light grey) increases substantially. Ge doped samples present Ge precipitate phases which increase proportionally to the dopant concentration. Also, slight amounts of SiC in samples a, and c – e, while sample b shows Si phase (green arrows) around the grain boundaries.

For the O 1s core-level spectrum Fig. 5, four components were needed to obtain the best fitting. Two components on the low binding energy side were assigned to Mn-oxide while the most intense peak is arising from the SiO_2 phase. The component with the highest binding energy could be associated with physi-sorbed water [34]. In Al-doped samples, components corresponding to Al-O could not be resolved due to very proximate binding energy with Mn-oxide components [37]. Ge doped sample revealed the presence of another component at 532.1 eV due to GeO_2 [36]. Deconvoluted O 1s spectra were evidence of an increase in the Mn-oxide phase with Al doping while a decrease with Ge doping. Analysis of Al 2p and Ge $2p_{3/2}$ core level region evidenced the presence of Al_2O_3 and GeO_2 in Al-doped and Ge-doped samples, respectively Fig. 6.

3.2. Isothermal oxidation

3.2.1. Effect of consolidation techniques

To investigate the effect of different consolidation techniques on the oxidation resistance, as-cast, HP sintered, and SPS $MnSi_{1.74}Ge_{0.01}$ alloys were oxidized at 300 °C, 350 °C, 400 °C, 450 °C, and 600 °C; isothermally treated in ambient air for 24 h, see Fig. 7. All samples had insignificant scale growth at low temperatures (<400 °C). For temperatures above 400 °C, the weight gradually increased. The as-cast specimens Fig. 7(a) showed an irregular weight gain for all temperatures with a total weight gain of 7.5 μg/mm^2 after 24 h at 600 °C. The HP sampled showed the highest weight increase for all temperatures, with a total weight gain of 29 μg/mm^2 after 24 h at 600 °C, while the SPS sample had much lower oxidation rates, with only a weight increase of 1.8 μg/mm^2 for the same test conditions. A slow weight loss was noticed for some of the samples oxidised at lower temperatures (Fig. 8(a)) especially below 450 °C. The weight loss is possibly due to adsorption/desorption of humidity, volatile compound CO, or CO_2 [38,39], due to variation in the humidity of the laboratory air used for the tests.

The effect of densification methods on oxidation was further investigated on pure HMS synthesized using “siligrain HQ Table 1” (a low purity 99.8 wt% Si feedstock) and densified by SPS and HP. Fig. 8(a) shows the weight gain of the SPS samples, with very small weight gains for all temperatures, with a total weight gain of 4.8 μg/mm^2 after 24 h at

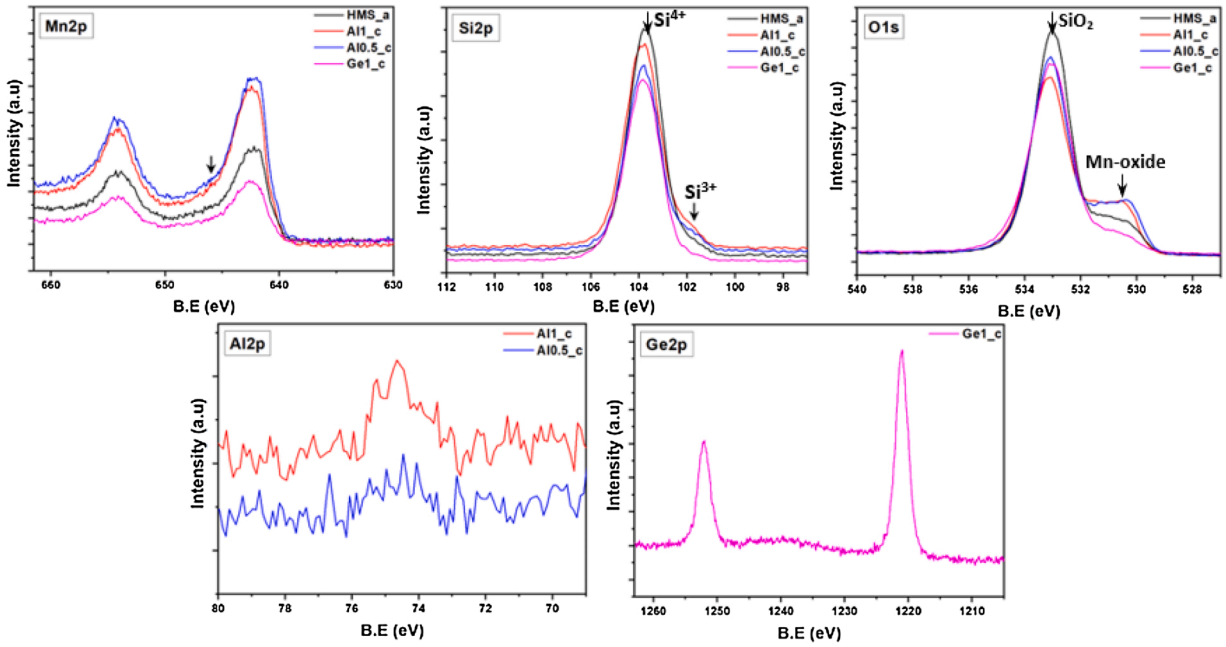

Fig. 3. X-ray photoemission spectra of the Mn 2p, Si 2p, O 1s, Al 2p, and Ge 2p core level regions.

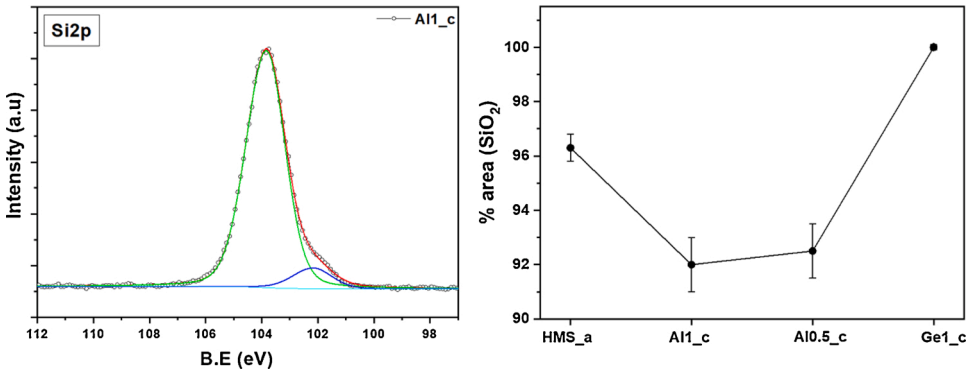

Fig. 4. Left panel: X-ray photoemission spectra of the Si 2p core level region with peak fitting results. Right panel: Integrated area for the SiO_2 component for undoped and doped samples.

600 °C, slightly higher than the SPS sample with a higher purity feedstock. However, for the HP sintered specimens (see Fig. 8(b)), the samples oxidized catastrophically at high temperatures up to two orders of magnitude higher than the SPS compounds. The catastrophic oxidation process occurred after initial cubic growth from 300 to 400 °C followed by linear growth at 450 °C and finally catastrophic oxidation above 600 °C. The latter was discussed by Branco N. P. [27], who defines cubic oxidation as a combination of linear and parabolic oxidation, which at higher temperatures becomes only linear and at further increased temperature the material oxidizes catastrophically.

Similarly, the cast and HP sintered specimen Fig. A1, presents the TGA data for the 0.5 at% Ge doped HMS ($MnSi_{1.745}Ge_{0.005}$) samples. The immediate observation is that this compound was more resilient towards oxidation than the 1 at% Ge doped HMS and pure HMS, and the scale growth (especially at low temperatures) was negligible below 500 °C.

3.2.2. *Composition effect*

The alloy composition has a major impact on oxidation kinetics, both due to the direct effect of dopants on the oxidation mechanisms, but also due to the effect of composition on the microstructure development and phase composition achieved during processing. Fig. A1(c) and Fig. 7(c) shows the 0.5 at% Ge and 1 at% Ge HMS doped HMS alloys, respectively, consolidated by SPS and heat-treated using a similar method. At temperatures below 400 °C, no significant effects of dopant type or concentration are seen. However, at 600 °C both the weight gain and the oxide thickness were much higher for the 1 at% Ge sample than the one containing 0.5 at% (see Fig. 9), corresponding to around 0.65 μg/mm^2 (or 248 nm thickness) and 1.7 μg/mm^2 (0.6 μm thickness). The same trend was noticed for HP samples and better confirmed by the low purity Si-based HMS Fig. 8. Unlike the Ge doped compounds, the siligrain-based alloys oxidized at low (300 °C) and high temperatures, the latter oxidized following parabolic model with rate constants of 0.616

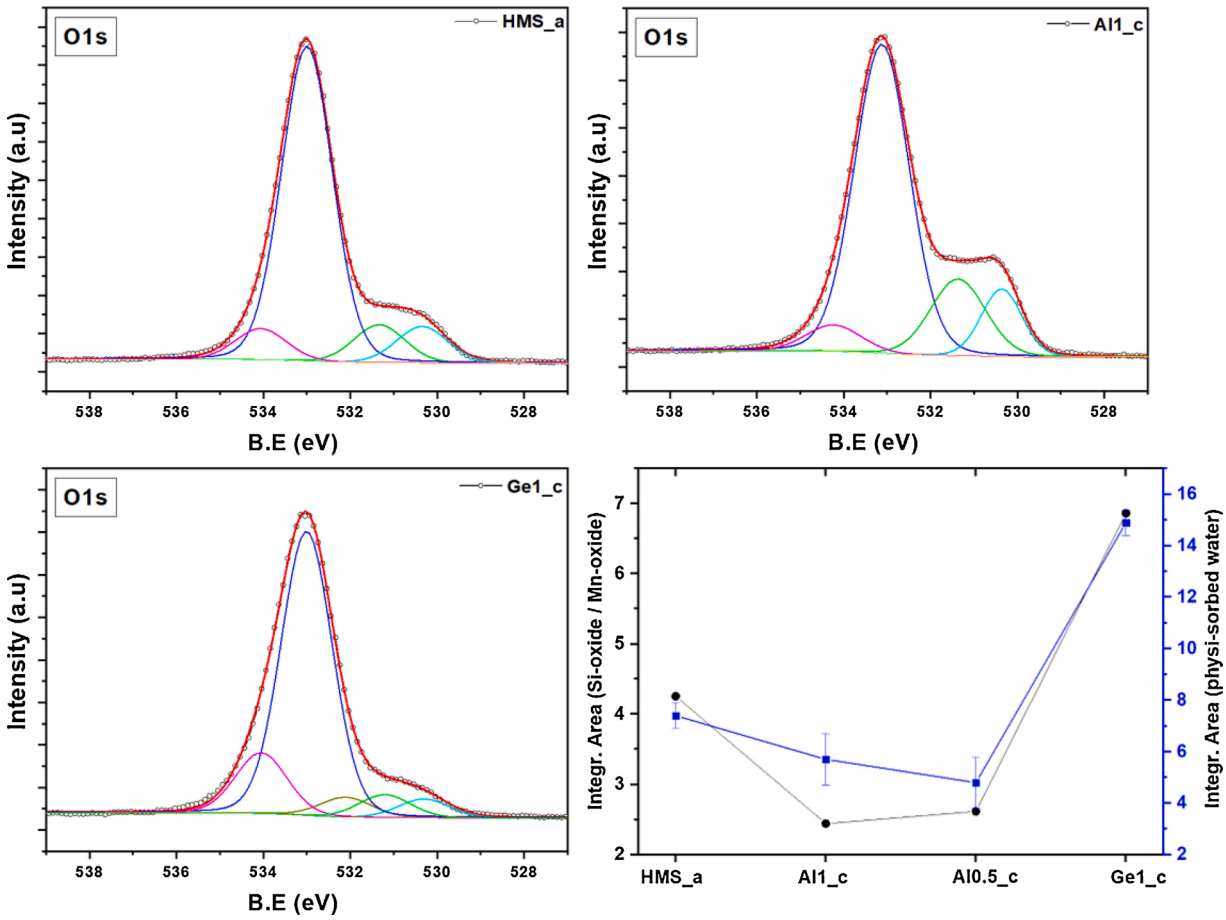

Fig. 5. X-ray photoemission spectra of the O 1s core level region with peak fitting results of HMS_a, Al1_c, and Ge1_c. Bottom right: Integrated area ratio of SiO2 component to Mn-oxide component for undoped and doped samples (in black). Integrated area for the component associated to physi-sorbed water is also shown (in blue).

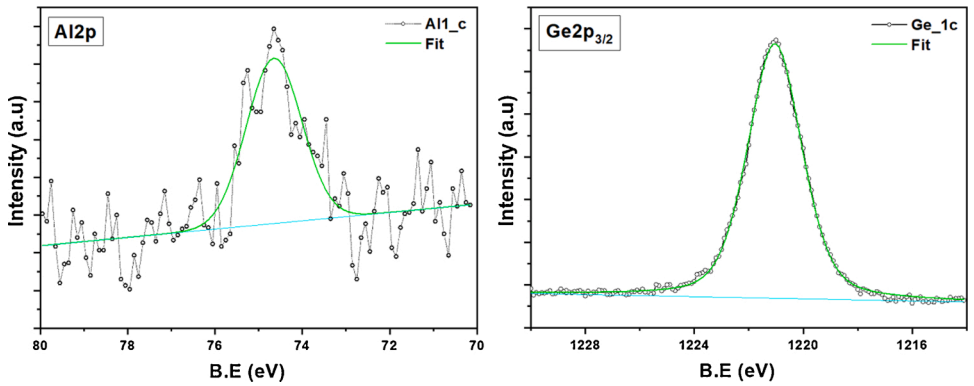

Fig. 6. X-ray photoemission spectra of the O 1s core level region with peak fitting results.

$\mu g^2/mm^4h$ and 2 $\mu g^2/mm^4h$, respectively. At high temperature, the compound based on less pure silicon oxidized with two orders of magnitude higher rate than the 0.5 at% Ge HMS (5.44 $\mu g^2/mm^4h$ oxidation rate). Thus, the higher the impurities/dopant the higher the oxidation potential and the behaviour agrees with the isoconversion results.

3.2.3. *Effect of humidity*

Long-term oxidation experiments were carried out on Ge doped specimens in ambient air for up to 200 h retention time, to investigate the oxidation mechanisms over time. Fig. 10(a), shows the weight change and relative heat flux of the Ge doped specimens in ambient air for up to 200 h retention time. The TGA curve reveals that the sample's oxidation occurs in periodic steps of 11 h weight gain and 13 h weight loss per cycle, while from the relative heat flux graph, the exothermic and endothermic behaviour alternates in line with the weight loss and gain, respectively. The weight gain and loss cyclic trend was identified over the entire period and reflected the difference in vapor pressure over the day (24 h). Where the observations showed that the mass gain occurred during the night and mass loss during the day with a very high

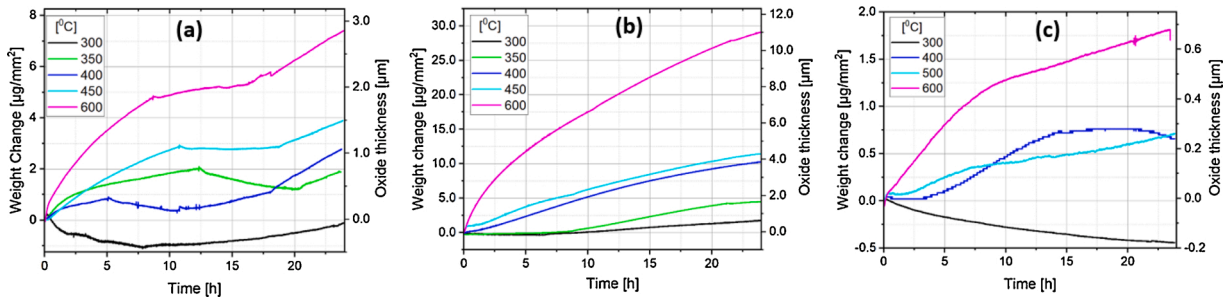

Fig. 7. Thermogravimetric weight change of 1at% Ge HMS alloys isothermally (temperature: 300 °C-600 °C) oxidized in laboratory air for 24 h, a) as-cast, b) milled and consolidated by HP, c) milled and consolidated by SPS.

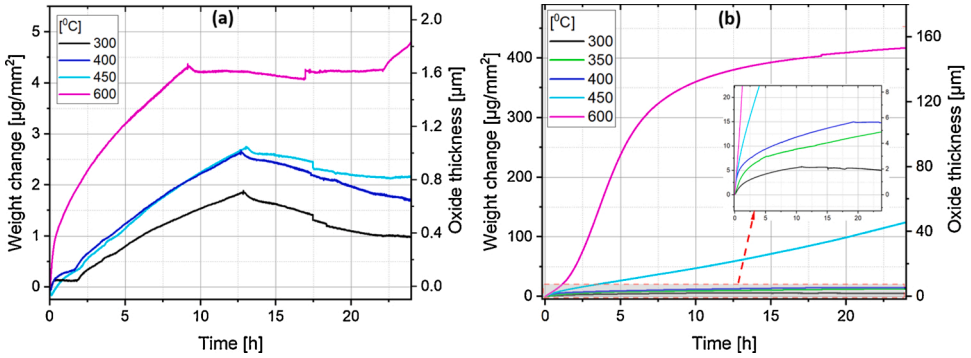

Fig. 8. Thermogravimetric analysis results of pure HMS synthesized from low purity Si feedstock, densified by a) SPS, b) HP; and heat-treated in air.

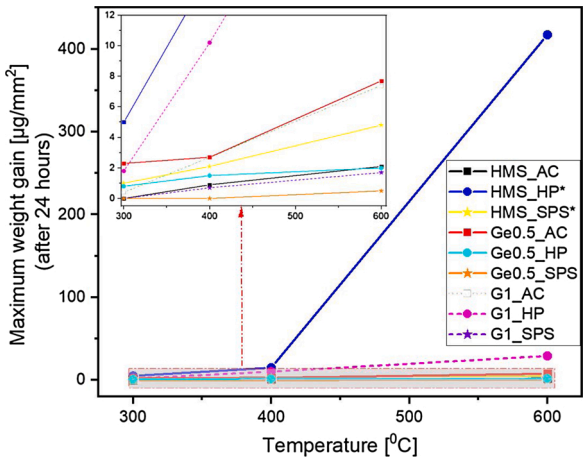

Fig. 9. Weight gain after 24 h isothermal oxidation at 300 °C, 400 °C and 600 °C. * are alloys synthesized from low purity silicon feedstock.

temperature drop during the night (~11 °C on average), and the level was even higher on one rainy evening where the relative humidity in the room was much higher than for a dry day. Finally, the weight gain segments occurred in two steps, the first consisting of the adsorption of oxygen at the alloy surface which initiates the diffusion of metal cations and formation of SiO_2 (α – quartz) oxide with a parabolic diffusion constant of 0.732 $\mu g^2/mm^4h$. While the second is characterized by a reduced diffusion rate of 0.21 $\mu g^2/mm^4h$ diffusion constant. The same trend was observed for all the cycles, though, with time the oxidizing agent diffusion constant gradually decreases, this is consistent with the notion that the scale grows slowly, and the oxidation rate decreases with time.

At higher temperature (600 °C), the reaction follows the same trend, though with longer weight gain segments than weight loss, as shown by Fig. 10(b). The exothermic reaction lasted 16 h, while the endothermic reaction lasted 8 h, which is contrary to the specimen run in ambient air, this time the mass gain lasted longer. On the other hand, the alloy was also heat treated in dry air at 400 °C Fig. 10(c), to investigate the oxygen partial pressure or humidity contribution on the oxidation of the 0.5 % Ge doped alloy. The TGA and DSC curves show a completely different trend in dry air compared to that in ambient air, and the scale size attained at 47 h in dry air is thicker than that reached in ambient air.

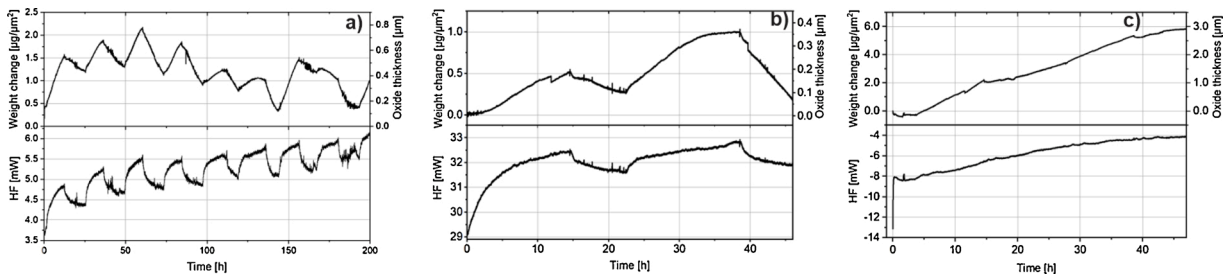

Fig. 10. Long-term TGA oxidation of 0.5at% Ge HMS consolidated by SPS, heat-treated: a) in air for 200 h at 400 °C, b) in air for 47 h at 600 °C, and c) in dry air for 47 h at 400 °C.

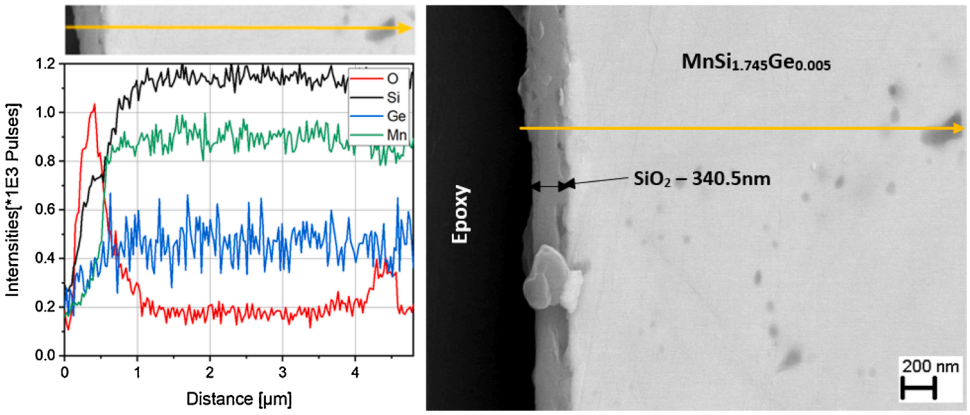

Fig. 11. SEM/EDS representation of $MnSi_{1.745}Ge_{0.005}$ (SPS consolidated) and oxidized at 400 °C for 200 h. (left) EDS line scan spectrum, (right) SEM image showing the cross-section of the interface between alloy and oxide scale layers.

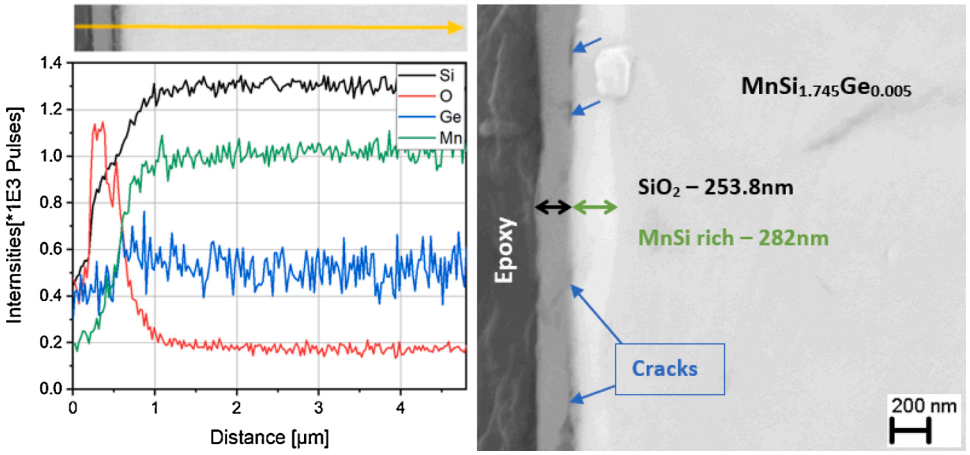

Fig. 12. SEM/EDS representation of $MnSi_{1.745}Ge_{0.005}$ (SPS consolidated) and oxidized at 600 °C for 50 h. (left) EDS lines can spectrum, (right) SEM image showing the cross-section of the interface between alloy and oxide scale layers.

Therefore, the heat treatment in dry air reveals that the weight losses are possibly due to physi-sorbed water (also seen by XPS) which forms in H_2O contained atmosphere with high vapor pressure.

3.3. Oxide scale crystal structure, morphology, and composition

SEM images of the cross section of the oxidised surface of the 0.5at% Ge doped sample is seen in Fig. 11 (400 °C, 200 h) and Fig. 12 (600 °C, 50 h). A thin layer of SiO_2 is visible for both samples, uniformly covering the entire surface. The thickness is around 340 nm for the sample oxidised at 400 °C for 200 h and 250 nm for the sample oxidised at 600 °C for 50 h. For the latter sample, also a 280 nm Mn-depleted layer is visible directly below the SiO_2 layer. Some cracks are also visible both between the layers and within the SiO_2 layer.

Moreover, Fig. 13 presents SEM micrographs of the cross-sections of $MnSi_{1.745}Ge_{0.005}$, heat-treated in the air for 24 h at 300 °C, 400 °C, and 600 °C. At 300 °C no trace of oxide scale was visualized even with high resolution. At 400 °C a SiO_2 scale was observed; however, the silicon depletion layer was smaller, and the scale was not uniform along the surface of the sample. Above 600 °C, both the Si depleted region and the scale could be distinguished, with more than half a micrometre oxide (0.5 μm) width. The oxide scale contained trace of Si-, Mn- and Ge-oxide based phases Fig. 13(c).

Fig. 14(a) shows the SEM/EDS elemental map (far right) of the HMS (based on low purity Si-feedstock) oxidized at 600 °C. The oxide is noticed on the grain boundaries, and some of the grains were fully oxidized. The oxide is mainly SiO_2 and partially Mn, and Fe-based. Fig. 14(b) presents a sample with similar composition densified by SPS. The EDS analysis shows that the oxidation robustness is improved with consolidation by SPS relative to the HP densification method, however, a long strip of MnO can also be noticed in the middle of the oxide. The diffusion of Mn^{2+} and Mn^{4+} cations through the scale-alloy interface, promoting the formation of MnO and MnO_2 oxides was a result of a nonprotective SiO_2 scale.

4. Discussion

4.1. Oxidation of pure HMS

HMS ($MnSi_{1.75}$) compounds synthesized from the more purified Si

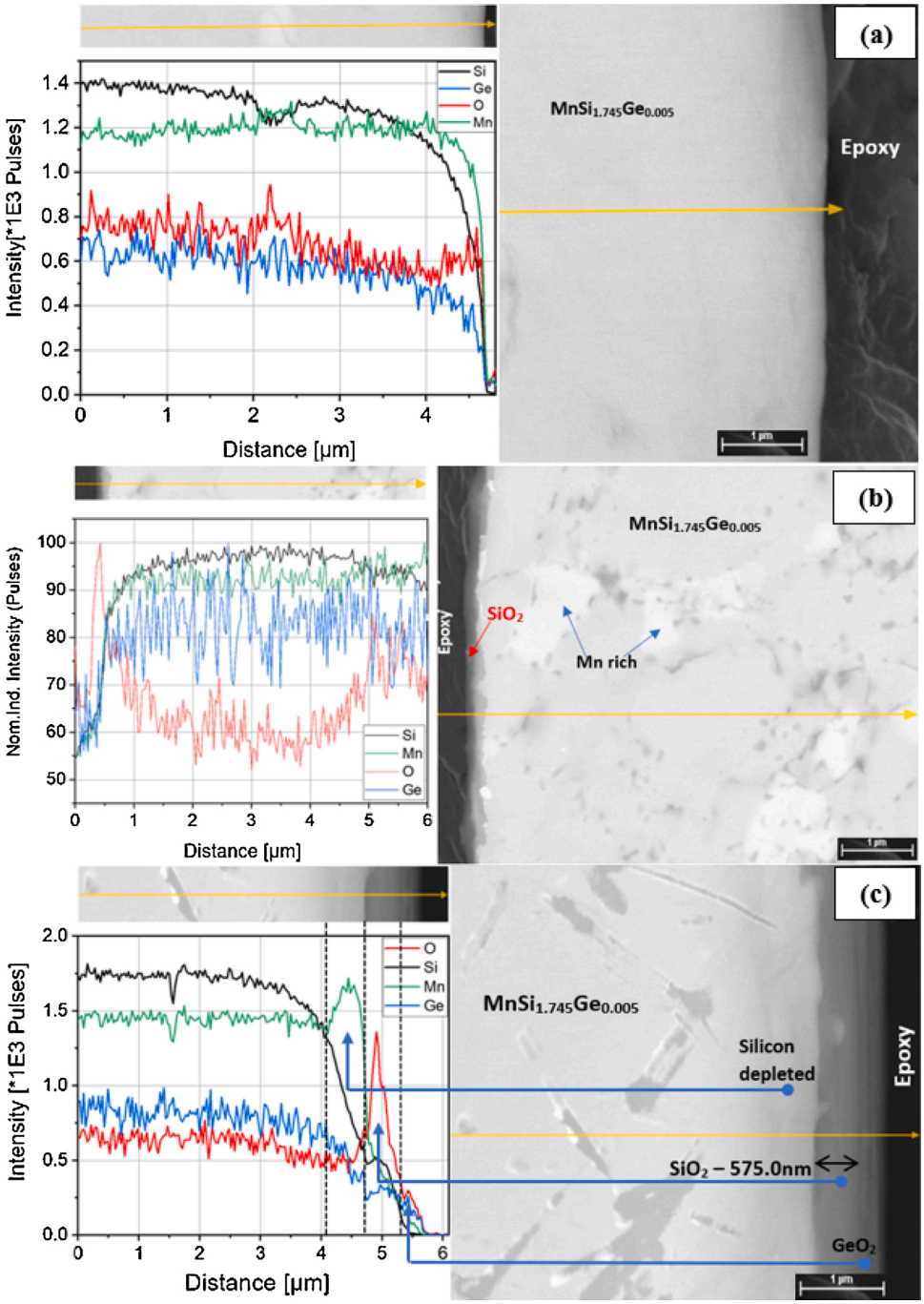

Fig. 13. Cross sectional comparison of the $MnSi_{1.745}Ge_{0.005}$ consolidated by Hot Press and oxidized at a)300 °C b)400 °C and c)600 °C in air for 24 h.

feedstock (see Table 1) were more robust to oxidation among all studied alloys. The alloy selectively grew SiO_2(α-quartz above 300 °C and β-quartz above 575 °C), where the silica oxide coexisted with a silicon depleted layer (see Fig. 16(1)). The alloy provides sufficient and gradual flux of Si to the specimen surface, developing an external silica oxide at the Alloy-Oxide interface. Carl Wagner [40], provided a necessary but not sufficient condition for the formation of an exclusive formation of one oxide in the case of metal "A" alloyed with "B", as shown by Eq. 4.

$$N_{B(\min)} = \frac{1}{16 Z_B c}\left(\frac{\pi k_{pB}}{D}\right)^{1/2} \quad (4)$$

Where: $N_{B(min)}$ – Minimum concentration of the alloying element, Z_B – Atomic number, c – number of gram-atoms of the metal per unit volume, π – the dissociation pressure of the oxide "BO", k_{pB} – the oxidation rate constant of the parabolic rate law and D - the interdiffusion coefficient.

Ning H. et al. [20] conducted oxidation experiments on $MnSi_{1.74}$, the specimen edge cross-section was composed of mainly SiO_2 and MnSi phases at 600 °C after 500 h, however, in the current study, XPS revealed that the oxide layer was also composed of minor Mn-oxide that originate from Mn^{2+} and Mn^{3+} oxidation states, though only at high temperature. In the initial stages of oxidation, Si preferentially oxidises and form a relatively dense and stable SiO_2. If the molar fraction of Si at the alloy-SiO_2 is close to minimum, the diffusion of O^{2-} ions through the SiO_2 layer will cause some oxidation of Mn at the interface, but due to the low diffusivity of O^{2-} in Mn-oxides this layer will not grow further.

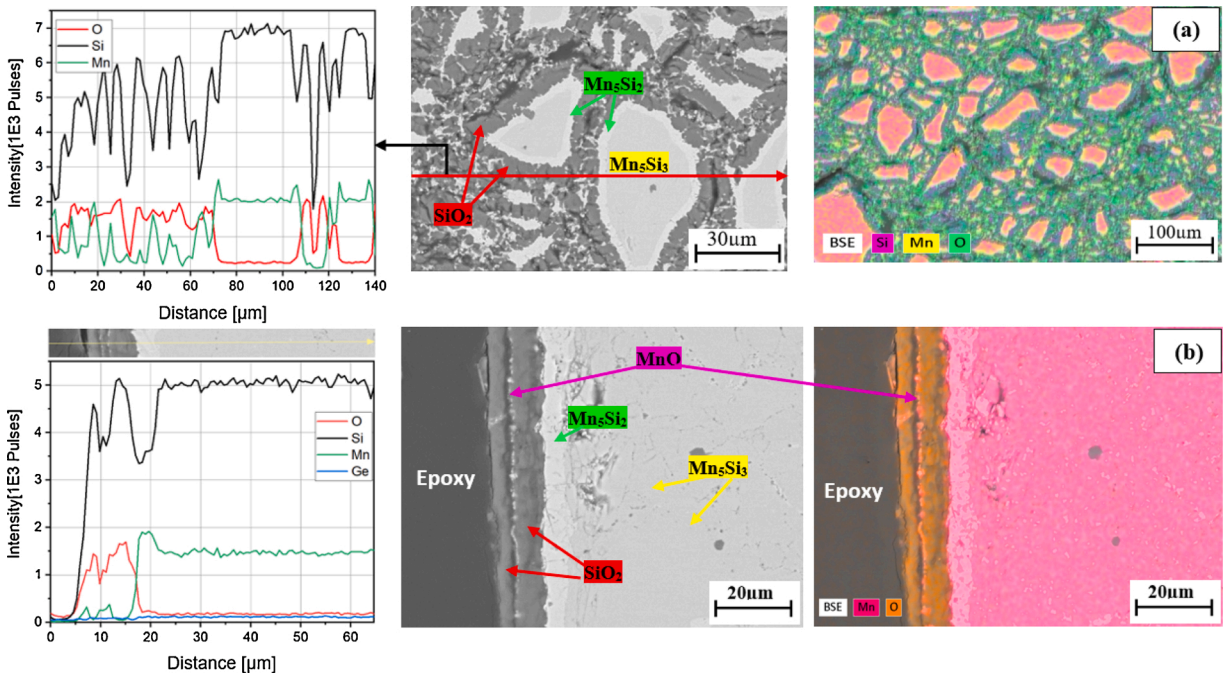

Fig. 14. Cross-sectional EDS composition analysis of pure HMS synthesized based on siligrain HQ (Si feedstock) and consolidated by a) Hot Press at 950 °C and b) SPS, both TGA oxidised at 600 °C for 24 h.

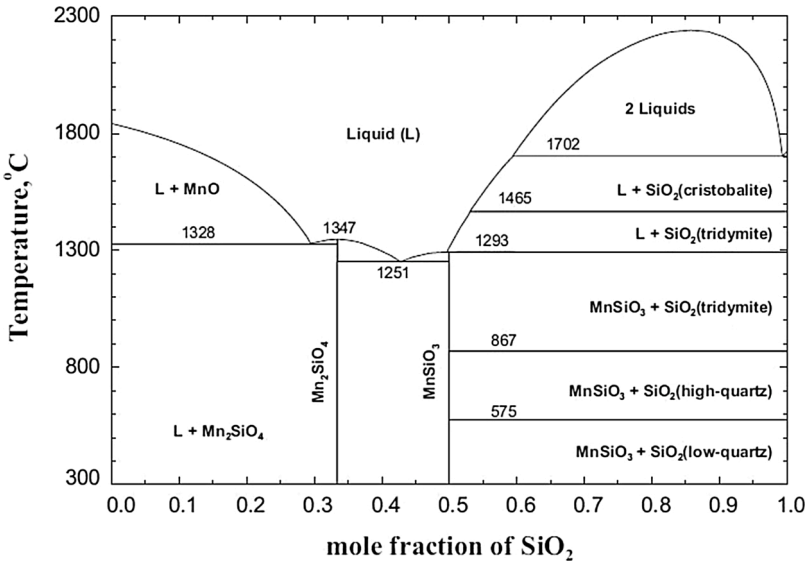

Fig. 15. Optimized Phase diagram of MnO-SiO_2 oxide phases [42].

Furthermore, the long-term coexistence of the formed oxides is a crucial stability deterministic factor. This was not thoroughly investigated by the current study, nevertheless, it was experimentally investigated by Robie R.A. et al. [41] and revealed that the $MnSiO_3$(rhodonite) crystalline phase was grown at 890 °C for 20 h thermal exposure. A similar observation was made using theoretic models (factsage.com [42] and FISHER model [43]) under MnO-SiO_2 phase equilibrium simulations as a minor phase, however, the manganese silicate ($MnSiO_3$) was not observed both at low and high (600 °C) temperatures in this study (Fig. 15).

4.2. Oxidation of doped HMS

Based on the kinetics of oxidation results (chapter 3), the doped alloys showed high potential to oxidation in comparison to the pure HMS. Comparatively, Ge-doped alloys were marginally distinct from the pure HMS than the Al-doped compounds as by the isoconversion (Fig. 1) and isothermal oxidation results. “Al” and “Si” were reported to be two among three elements that, by selective oxidation form a slow-growing and protective scale [44] together with chromium. From the high molar concentration of silicon (Si) in the alloys, Si preferentially has higher

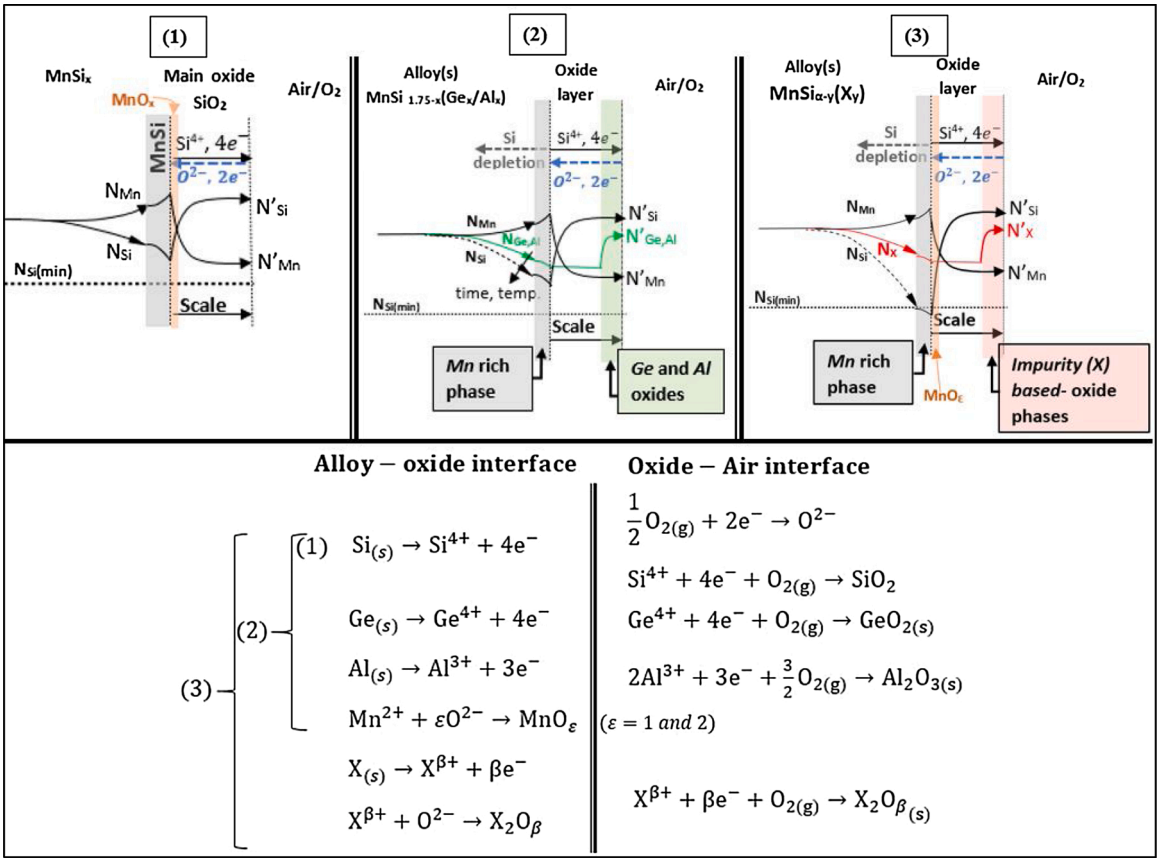

Fig. 16. Schematic overview of the HMS (pure or doped) oxidation profile showing "the main scenarios" of Si diffusion through the oxide scale and its inward depletion. The material transport is subdivided in three categories: (1) $N_{Si}>N_{Si(min)}$ – selective oxidation, usually for undoped HMS or doped HMS (for short retention time or below 500ºC), Mn oxide is little to none and SiO2 protective; (2) $N_{Si}>N_{Si(min)}$ – similar to (1) though at longer period or high temperature at low dopant concentration; (3) $N_{Si}<N_{Si(min)}$ (Nonprotective) all elements are involved starting from the most reactive to oxidation (formation of a conglomerate of oxides).

thermodynamic activity or higher affinity to oxidation relative to other elements. As schematically illustrated in Fig. 16 , initially, the oxidant (air) is adsorbed at the alloy surface; with temperature, high energy electrons on the silicon atom are knocked out and creates a Si^{2+} cation defect, as a result, the silica layer nucleates and grows continuously at a very slow rate ($0.23\mu g^2/mm^4h$ at 400 °C). The scale coexists with a silicon depleted layer, with which as silicon is consumed close to the oxide alloy interface, Ge relative activity increases inversely proportional to the Si diffusion rate, preferentially above 600 °C. As a result, a Ge based oxide nucleates a GeO_2 oxide. Similar mechanisms apply to the Al-doped compound which exhibited Al_2O_3 among oxides, though at a distinct rate. Moreover, it was noticed (by the XPS analysis) that at high temperature the stability of the Al-doped alloy is compromised as the level of Mn-oxide increase relative to the Ge doped or pure HMS. This reveals and confirms that Ge along with Si oxides is more protective than with alumina, where Fig. 4 (right panel) shows that with Ge-doping the oxide scale is almost solely SiO_2.

The thermal oxidation robustness of HMS is unquestionable below 600 °C and this study has proven the case. However, it was also revealed that the oxidation resistance of HMS does not rely only on the stoichiometry but also depends on the densification method, the dopant type, and the purity of the raw materials feedstock. This was seen when comparing the oxidation rate of as-cast, HP, and SPS material. With HP the specimen oxidised at a very high rate, especially at high temperature. The main cause is the weak mechanical strength between particles such that oxidation can occur easily along grain boundaries of non-completely sintered grains, as evident from Fig. 14(a) and Fig. A4, and also seen from physical images of the samples Fig. A2 thermally oxidized for 24 h, where the oxides increased the volume of the specimen till it disintegrated. In contrast, the SPS consolidated specimen Fig. 14(b) at 600 °C shows that the internal oxidation is greatly reduced, and all oxidation occurs at the surface following more standard scale growth diffusion kinetics. Hence, the mechanical integrity of the sample showed huge advantages in reducing the oxidation of the compounds, mainly because of reduced surface to volume ratio exposed to heat and oxidation agent(s).

The effect of dopants and impurities on the oxidation rate is also clearly seen and the mechanisms underlaying this is summarised in Fig. 16, dividing it roughly into three different groups: (1) Pure HMS oxidation for short and long retention time, or low dopant/impurity concentration for short retention time, (2) higher temperature or longer exposure at low dopant/impurity concentration, and (3) high dopant/impurity concentration leading to non-protective oxide scale growth.

Case (1) was seen mainly for undoped HMS samples, where the mechanism of oxidation is governed by "Si" selective oxidation to SiO_2 and further details were discussed in section 4.1 above.

Case (2) was observed for doped HMS alloys. With Ge and Al as dopants, transient GeO_2 and Al_2O_3 oxides grow at the same time as SiO_2

(though relatively faster). As shown in Fig. 16(2), overtime a continuous silica layer is formed with respective Ge- and Al-oxides at the SiO_2 - Air interface. At temperature below 400 °C (see Fig. 11), the depletion layer is very small after 200 h of oxidation time, revealing the SiO_2 passivity at this temperature and justifying the lack of Mn oxide with XPS characterisation. However, at 600 °C a wide silicon depleted layer is witnessed on the alloy side of the interface (see Fig. 12), and the alloy presented crucks at the alloy-oxide interface. With reduced Si molar fraction at the alloy side, the stresses were a result of compositional changes at the alloy-oxide interface and can also be linked to compressive stress between MnSi and SiO_2 phases. Over time, the alloy oxidation mechanisms could shift to as represented by Fig. 16(3). The latter would lead to the formation of Mn-based oxide(s) and compromise the SiO_2 protectiveness.

Case (3) was seen mainly on alloys with high dopant/impurity concentration. HMS sample synthesized from more impure silicon feedstock showed slow (cubic) oxidation at temperatures below 400 °C, at 450 °C temperature the compound oxidizes linearly, and finally, at high temperature, it oxidizes catastrophically (see Fig. 8(b)). This kinetics of oxidation is a result of nucleation of a conglomerate of oxides that form based on the impurities (Fe, Al, B, etc) and nucleate in parallel with silica, therefore compromising the protectiveness of silica. Though the mechanisms leading to catastrophic oxidation was out of the article's scope, it is represented in the same angle as the high temperature oxidation by scenario three (see equations of both oxide interfaces Fig. 16).

The three cases presented above are only valid for atmospheres where $O_2(g)$ is the dominant oxidation species. However, after long term oxidation tests in laboratory (humid) air Fig. 10(a), it was noticed that the effect of humidity should also be considered. In a water contained atmosphere, H_2O is adsorbed on SiO_2 and react to form silicon hydroxide ($Si(OH)_{4(s)}$ Eq. 5, also reported by Copland E. et al. [45] in the temperature range of 300 °C–600 °C. The nucleated hydroxide will reach an equilibrium concentration "K" (Eq. 6) where it slows down both Si^{2+} and O^{2-} diffusion (meanwhile the oxidation rate). The stability of $Si(OH)_4$ (also reported by [46]) is reached under certain H_2O partial pressure (pH_2O) in the atmosphere. Simultaneously due to varying pH_2O, some $Si(OH)_{4(s)}$ dissociates following Eq. 5 and H_2O vaporises, which is witnessed in the weight loss sections, see Fig. 10(a). Towards the night, the silica formation is again resumed under reduced pH_2O and the cycle continues.

$$SiO_{2(s)} + 2H_2O_{(g)} \leftrightarrow Si(OH)_{4(s)} \quad (5)$$

$$K = \frac{a_{Si(OH)_4}}{pH_2O \times a_{SiO_2}} \quad (6)$$

Where $a_{Si(OH)_4}$ – is the local (oxide-air interface) molar fraction of $Si(OH)_4$, a_{SiO_2} – is the local molar fraction of SiO_2. Further studies could extensively investigate the effect of H_2O on the stability of SiO_2, pertaining to oxidation of HMS.

5. Conclusion

High temperature oxidation of $MnSi_{1.75-\alpha}X_\alpha$ was investigated in this article. The alloys showed robustness to oxidation at temperatures below 500 °C forming a SiO_2 protective layer. However, the formation of SiO_2 layer mechanisms was studied and the level of protectiveness was discussed.

At temperature above 600 °C, the rate of outward diffusion of Si ions at the alloy-oxide interface is higher than that from the core. That affects much the oxidation kinetics, with the formation of third element-based oxides (Al_2O_3 and GeO_2) and Mn-oxides, which coexist with the main oxide (SiO_2) and reduce its protectiveness.

At temperature below 500 °C, the oxidation rate is reduced and with time (as seen after 200 h of isothermal exposure), a compact and continuous layer of SiO_2 is formed at the alloy edges with GeO_2 (for Ge doped HMS) at the oxide-gas interface. Moreover, all other oxides were found to be quantitatively minor to SiO_2 for alloys with pure Si-feedstock (purity >99.999 wt%).

XPS composition analysis revealed that with Ge doping the Mn-oxide was quantitatively reduced than with Al doping by a difference of almost 8% (considering 1at% doping on both sides). Therefore, $GeO_2 – SiO_2$ was a more protective combination than with Al_2O_3. Moreover, this study found that alloys with 0.5at% dopant concentration were more resistant to oxidation, and in case of excessive doping, both the kinetics and mechanisms of oxidation of HMS alloys are considerably affected.

The oxidation kinetics and mechanisms are also dependent on the mechanical integrity of the alloys. The samples densified by hot pressing had 3 times more weight gain than as-cast samples, while with SPS the oxidation resistance was much better than the others.

Finally, at worst scenario coupling excessive doping (or more impurities) with HP consolidation method, the alloys oxidized at the grain boundaries, and lead to catastrophic oxidation. Therefore revealing the important relationship between oxidation potential, impurities optimisation, and density of alloys.

Declaration of Competing Interest

The authors report no declarations of interest.

Data availability

Data used in this manuscript will be made available by the corresponding author upon reasonable request.

CRediT authorship contribution statement

Antoine de Padoue Shyikira: Conceptulization, Data curation, Formal analysis, Investigation, Methodology, Project administration, Validation, Writing - original draft, Writing - review & editing. **Naureen Akhtar:** Methodology, Investigation, Validation, Formal analysis, Writing - original draft. **Gunstein Skomedal:** Conceptualization, Methodology, Supervision, Writing - review & editing. **Tor Oskar Sætre:** Supervision. **Peter Hugh Middleton:** Supervision, Writing - review & editing.

Acknowledgments

The author would like to acknowledge all partners: Elkem ASA, Sintef, and the University of Oslo (UiO) in TESil project, for their help form material synthesis, pellet consolidation, and transport properties tests. Moreover, the authors would like to appreciate Prof. Spyros Diplas tremendous contribution to conducting the XPS tests. Finally, we acknowledge financial support from the Research Council of Norway (Project No 269326).

Appendix

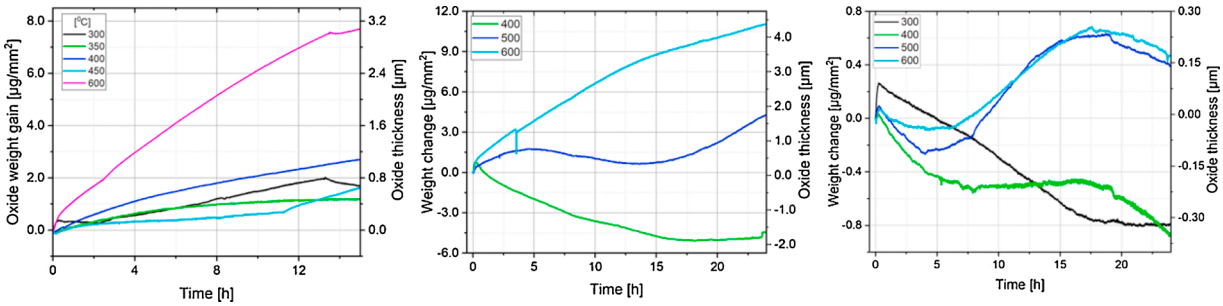

Fig. A1. Thermal gravimetric weight change of 0.5at% Ge HMS alloy in laboratory air, a) as-cast, b) milled and consolidated by HP, c) milled and consolidated by SPS.

Fig. A2. Isothermal oxidation of Siligrain based pure HMS, HP consolidated in laboratory air. Specimen at 450 °C and 600 °C considerably increased in volume and the reaction was driven with 4.82 kJ/mol activation energy.

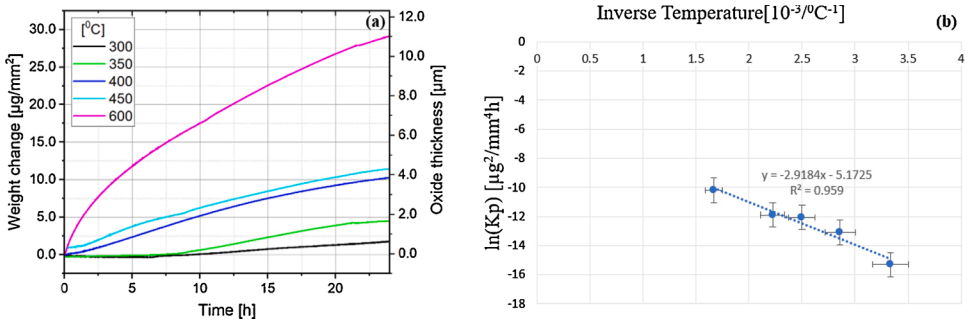

Fig. A3. (a)Weight gain over time of 1at% Ge doped HMS, densified by HP and heat treated in Dry Air at temperatures ranging from 300 °C to 600 °C, (b) An illustration of how the parabolic oxidation rate constant k_p was approximated by Arrhenius plot/model. The natural logarithm of k_p is plotted against reciprocal temperature.

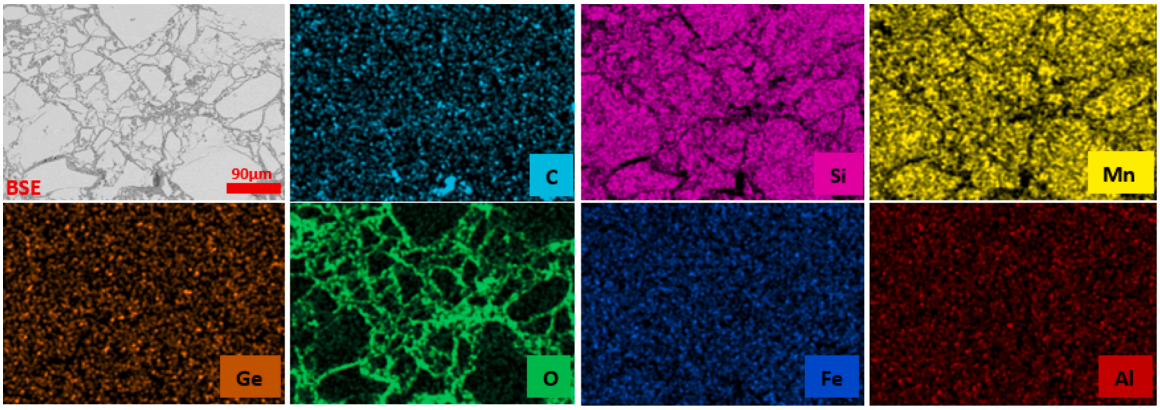

Fig. A4. Elemental mapping by SEM-EDS of the pure HMS synthesized based on siligrain (as a Si feedstock), oxidized at 450 °C for 15 h in Air.

References

[1] D.M. Rowe, CRC Handbook of Thermoelectrics, CRC Press, Cardif, Wales, 1995. Boca Raton.
[2] Z. Zamanipour, X. Shi, M. Mozafari, J.S. Krasinski, L. Tayebi, D. Vashaee, Synthesis, characterization, and thermoelectric properties of synthesis, characterization, and thermoelectric properties of nanostructured bulk p-type $MnSi_{1.73}$, $MnSi_{1.75}$, and $MnSi_{1.77}$, Ceram. Int. 39 (2021) 2353–2358, https://doi.org/10.1016/j.ceramint.2012.08.086, 2. 13.
[3] A. Nozari, P. Norouzzadef, F. Suarez, D. Vashaee, Thermoelectric silicides: a review, J. Appl. Phys. 56 (May) (2017) 1–27.
[4] D.Y.N. Truong, Thermoelectric Properties of Higher Manganese Silicides, University of Waterloo, Ontario, 2015.

[5] I. Aoyama, H. Kaibe, L. Rauscher, T. Kanda, M. Mukoujima, S. Sano, T. Tsuji, Manganese silicides (HMSs, $MnSi_{1.74}$) and characterization of thermoelectric generating module using p-type (Al, Ge and Mo)-doped HMSs and n-Type $Mg_2Si_{0.4}Sn_{0.6}$ legs, J. Appl. Phys. 44 (2005) 4275–4281, https://doi.org/10.1143/JJAP.44.4275.

[6] W. B. a. F. Gillen, Process of making Mn_4Si_7 thermoelectric element and product of said process, USA Patent (Oct (22)) (1968), 3407037.

[7] D.Y.N. Truong, H. Kleinke, F. Gascoin, Preparation of pure higher manganese silicides through wet ball milling and reactive sintering with enhanced thermoelectric properties, Intermetallics 55 (2015) 127–132, https://doi.org/10.1016/j.intermet.2015.07.002.

[8] G. Kima, H.J. Rima, K.H. Lee, J.W. Roh, W. Lee, Suppressed secondary phase generation in thermoelectric higher manganese silicide by fabrication process optimization, Ceram. Int. 45 (2019) 19538–19541, https://doi.org/10.1016/j.ceramint.2019.06.104.

[9] S. Perumal, S. Gorsse, U. Ail, M. Prakasam, P. Rajasekarb, A.M. Umarji, Enhanced thermoelectric figure of merit in nano-structured Si dispersed higher manganese silicide, Mater. Sci. Semicond. Process. 104 (2019), https://doi.org/10.1016/j.mssp.2019.104649.

[10] W. Luo, H. Li, F. Fu, W. Hao, X. Tang, Improved thermoelectric properties of Al-doped higher manganese silicide prepared by a rapid solidification method, J. Electron. Mater. 40 (5) (2011) 1233–1237.

[11] A.J. Zhou, T.J. Zhu, X.B. Zhao, S.H. Yang, T. Dasgupta, C. Stiewe, R. Hassdorf, E. Mueller, Improved thermoelectric performance of higher manganese silicides with Ge additions, J. Electron. Mater. 39 (9) (2010) 2002–2007.

[12] H. Lee, G. Kima, B. Lee, J. Kima, S.-M. Choi, K.H. Lee, W. Lee, Effect of Si content on the thermoelectric transport properties of Ge-doped higher manganese silicides, Scr. Mater. 135 (2017) 72–75, https://doi.org/10.1016/j.scriptamat.2017.03.011.

[13] P. Dharmaiah, C.-hee Lee, G. Song, S.-J. Hong, Mechanical and thermoelectric properties of environment friendly higher manganese silicide fabricated using water atomization and spark plasma sintering, Intermetallics 119 (2020), https://doi.org/10.1016/j.intermet.2020.106705.

[14] X. She, X. Su, H. Du, T. Liang, G. Zheng, Y. Yan, R. Akram, C. Uherb, X. Tang, High thermoelectric performance of higher manganese silicides propared by ultra-fast thermal explosion, J. Mater. Chem. C 3 (2015) 12116–12122, https://doi.org/10.1039/c5tc02837j.

[15] H. Nagai, M. Okabayashi, Deleterious effect of Ti addition on the oxidation resistance of Ni-20Cr alloy, Trans. Japan Inst. Met. 22 (10) (1981) 691–698.

[16] E. Anzini, N. Glaenzer, P.M. Mignanelli, M.C. Hardy, H.J. Stone, S. Pedrazzini, The effect of manganese and silicon additions on the corrosion resistance of a polycrystalline nickel-based superalloy, Corros. Sci. 176 (2020).

[17] H. Yu, S. Ukai, S. Hayashi, N.H. Oono, Effect of Cr and Y_2O_3 on the oxidation behavior of Co-based oxide dispersion strengthened superalloys at 900 °C, Corros. Sci. 127 (2017) 147–156.

[18] S. Okada, T. Shishido, M. Ogawa, F. Matsukawa, Y. Ishizawa, K. Nakajima, T. Fukuda, T. Lundstrom, MnSi and $MnSi_{2-x}$ single crystals growth by Ga flux method and properties, J. Cryst. Growth 229 (2001) 532–536.

[19] G. Skomedal, A. Burkhov, Ar Samunin, R. Haugsrud, P.H. Middleton, High temperature oxidation of Mg_2(Si-Sn), Corros. Sci. (2016).

[20] H. Ning, M.J. Reece, F. Smeacetto, M. Salvo, Oxidation protective glass-ceramic coating for higher manganese silicide thermoelectrics, J. Mater. Sci. 51 (2016) 9484–9489.

[21] R. Funahashi, Y. Matsumura, T. Barbier, T. Takeuchi, R.O. Suzuki, S. Katsuyama, A. Yamamoto, H. Takazawa, E. Combe, Durability of silicide-based thermoelectric modules at high temperatures in air, J. Electron. Mater. 44 (8) (2015) 2946–2952.

[22] M. Salvo, F. Smeacetto, F. D'Isanto, G. Viola, P. Demitri, F. Gucci, M.J. Reece, Glass-ceramic oxidation protection of higher manganese silicide thermoelectrics, J. Eur. Ceram. Soc. (2018), https://doi.org/10.1016/j.jeurceramsoc.2018.01.007.

[23] Xiao-jiang Liu, Yong-quan He, Guang-ming Cao, Tao Jia, Teng-zhi Wu, Zhen-yu Liu, Effect of Si content and temperature on oxidation resistance of Fe-Si alloys, J. Iron Steel Res. Int. 22 (3) (2015) 238–244.

[24] D.J. Young, High Temperature Oxidation and Corrosion of Metals, Elsevier, Amsterdam, 2016.

[25] Elkem, "Thermoelectric Silicides," Elkem, [Online]. Available: https://www.elkem.com/innovation/research-projects/tesil/.

[26] N.B. Pilling, R.E. Bedworth, Oxidation of metals at high temperature, J. Inst. Met. 29 (1923), p. 529.

[27] B.N. Popov, Corrosion Engineering, Elsevier, Columbia, 2015.

[28] G. Lablanche, U.F. Volkert, G. Eggeler, E.P. George, Oxidation behavior of the CrMnFeCoNi hing-entropy alloy, Oxid. Met. 85 (2016) 629–645.

[29] G. Xie, X. Liu, Q. Li, H. Lin, Y. Li, M. Nie, L. Qin, The evolution of a-MnO_2 from hollow cubes to hollow spheres and their electrochemical performance for supercapacitors, J. Mater. Sci. 52 (18) (2017) 10915–10926.

[30] Zhi-Qiang Zou, Gao-Ming Shi, Li-Min Sun, Xiao-Yong Liu, Manganese nanoclusters and MnSi~1.7 nanowires formed on Si(110): a comparative x-ray photoelectron spectroscopy study, J. Appl. Phys. 113 (2013) 1–5.

[31] M.C. Biesinger, B.P. Payne, A.P. Grosvenor, L.W.M. Lau, A.R. Gerson, R.St. C. Smart, Resolving surface chemical states in XPS analysis of first row transition metals, oxides and hydroxides: Cr, Mn, Fe, Co and Ni, Appl. Surf. Sci. 257 (2011) 2717–2730.

[32] H. Sun, X. Qin, F. Zaera, Chemical nature of the thin films that form on SiO_2/Si (100) surfaces upon manganese deposition, J. Phys. Chem. Lett. 2 (20) (2011) 2525–2530.

[33] A. Thogersen, J.H. Selj, E.S. Marstein, Oxidation effects on graded porous silicon anti-reflection coatings, J. Electrochem. Soc. 159 (5) (2011) 1–7.

[34] E.S. Ilton, J.E. Post, P.J. Heaney, F.T. Ling, S.N. Kerisit, XPS determination of Mn oxidation states in Mn (hydr)oxides, Appl. Surf. Sci. 366 (2016) 475–485.

[35] A. Barrera, F. Tzompantzi, J. Campa-Molina, J.E. Casillas, R. Pérez-Hernández, S. Ulloa-Godinez, C. Velásquez, J. Arenas-Alatorre, Photocatalytic activity of Ag/Al_2O_3–Gd_2O_3 photocatalysts prepared by the sol–gel method in the degradation of 4-chlorophenol, RSC Advance 8 (2018) 3108–3119.

[36] K. Prabhakaran, T. Ogino, Oxidation of Ge(100) and Ge(111) surfaces: an UPS and XPS study, Surf. Sci. 325 (3) (1995) 263–271.

[37] A.H. Alshehri, K. Mistry, V.H. Nguyen, K.H. Ibrahim, D. Muñoz-Rojas, M. Yavuz, K. P. Musselman, Quantum-tunneling metal-insulator-metal diodes made by rapid atmospheric pressure chemical vapor deposition, Adv. Funct. Mater. 29 (7) (2018).

[38] J.Y. Wang, X.M. Duan, Z.H. Yang, D.C. Jia, Y. Zhou, Ablation mechanism and properties of SiC/SiBCN ceramic composites under an oxyacetylene torch environment, Corros. Sci. 82 (2014) 101–107.

[39] L.Y. Xiang, L.F. Cheng, X.M. Fan, L. Shi, X.W. Yin, L.T. Zhang, Effect of interlayer on the ablation properties of laminated HfC-SiC ceramics undrer oxyacetylene torch, Corros. Sci. 93 (2015) 172–179.

[40] C. Wagner, Theoretical analysis of the diffusion processes determining the oxidation rate of alloys, J. Electrochem. Soc. 99 (1952) 369–380.

[41] R.A. Robie, S. Russell-Robinson, H.T. Evans, Flux growth of $MnSiO_3$ (rhodonite) crystals, J. Cryst. Growth 94 (1989) 981–982.

[42] Young-Min Kim, In-Ho Jung, Thermodynamic evaluation and optimization of the MnO-B_2O_3 and MnO-B_2O_3-SiO_2 systems and its application to oxidation of high-strength steels containing boron, Miner. Met. Mater. Soc. ASM Int. 46A (2015) 2736–2747.

[43] Y. Liu, S. Liu, X. Su, H. Peng, J. Wang, H. Tu, Calculation of selective oxidation in grain an grain boundary, J. Phase Equilibria Diffus. 34 (2) (2013) 82–88.

[44] N. Birks, G.H. Meier, F.S. Péttit, Introduction to The High-Temperature Oxidation of Metals, Cambridge University Press, New York, 2006.

[45] E. Copland, D. Muers, E.J. Opila, N.S. Jacobson, Thermodynamics of silicon-hydroxide formation in H2O containing atmospheres. High Temperature Corrosion and Materials Chemistry III, 1994.

[46] A. Hashimoto, The effect of H20 gas on volatilities of planet-forming major elements: I. Experimental determination of thermodynamic properties of Ca-, Al-, and Si-hydroxide gas molecules and its application to the solar nabula, Geochim. Cosmochim. Acta 56 (1992) 511–532.